# Varying ocean wave statistics emerging from a single energy spectrum in an experimental wave tank

Maxime Canard, Guillaume Ducrozet, Benjamin Bouscasse

Maxime Canard, Guillaume Ducrozet, Benjamin Bouscasse. Varying ocean wave statistics emerging from a single energy spectrum in an experimental wave tank. Ocean Engineering, 2022, 246, pp.110375. 10.1016/j.oceaneng.2021.110375 . hal-03546130

# Varying ocean wave statistics emerging from a single energy spectrum in an experimental wave tank

Maxime Canard[a,*], Guillaume Ducrozet[a], Benjamin Bouscasse[a]

[a] *Ecole Centrale Nantes, LHEEA Laboratory (ECN and CNRS), 1 rue de la Noë, 44000 Nantes, France*

---

## Abstract

As it strongly impacts the design of offshore structures, the realistic reproduction of sea states in experimental and numerical wave tanks is of great interest to the ocean engineering community. The vast majority of wave qualification procedures rely on the accurate control of i) the wave energy spectrum and ii) the wave crest statistics at a target location in the domain. However the control of the wave field is strongly challenged by nonlinear phenomena such as breaking and high-order nonlinearities, which are at the origin of significant variations of the wave properties along the tank. Considering this issue, the most common industry methodologies focus on reproducing the wave energy spectrum at the target position. The wave crest statistics are compared to reference distributions. The present study aims to explore the limitations of such a practice, investigating in detail the wave field properties for various target locations over a long domain. We address the problem within the framework of deep water long-crested irregular waves. In this respect, using the Ecole Centrale de Nantes (ECN) experimental facility, a specific sea state is consecutively generated at three positions of the wave tank using a dedicated procedure based on wave maker motion iterative corrections. For such

---

[*] Corresponding author

*Preprint submitted to Ocean Engineering* *November 2, 2021*

nonlinear wave conditions the wave crest statistics are known to be enhanced along the tank by high-order nonlinearities. As a result, configurations characterized by identical wave spectra lead to the generation of different wave crest distributions, revealing an increasing number of extreme events as the spectrum is generated farther from the wave maker. The data yielded by the study provide convincing evidence that controlling the wave field at a target location by correcting the sole energy spectrum is insufficient. Particular attention must be paid to the nonlinear spatial dynamics of the wave field in order to control the wave crest statistics.

---

## 1. Introduction

The response of offshore structures or ships to waves is an important part of assessing their safety in facing the design environmental conditions. The control of irregular wave fields in numerical or experimental wave tanks is thus of great interest to the ocean engineering community. The seakeeping tests are performed either at model scale (in an experimental or numerical wave tank) or at full scale (usually possible in a numerical domain only). The waves generated for such tests should i) represent realistic wave conditions and ii) contain the events leading to the extreme responses of the structure.

Wave conditions are defined through the notion of design sea states, established with methodologies given by the classification societies generally through a spectrum shape and a set of parameters (significant wave height $H_s$ and peak period $T_p$) (Det Norske Veritas, 2010; ITTC, 2011). They depend on the location of the ship or infrastructure and its life expectancy. The meteocean data will then provide the set of sea states that defines together with the wind and current, the environmental conditions that the ship or structure needs to sustain typically for the duration of a storm. For a common duration of 3 hours, and typical peak period values, the floating body will encounter around 1000 waves; and consequently the most extreme event to be considered will occur with a probability $P_{\text{design}} = 10^{-3}$.

On those grounds, two main approaches are used in engineering to account for the design sea sates.

First, deterministic procedures consist in generating a design wave, which is a short sequence of waves representative of the sea state. Each design wave is associated with a given probability level $P_{\text{design}}$. The shape of the generated wave packets is built using rare event probability tools. They depend on the sea state considered and the desired $P_{\text{design}}$ (Jensen and Capul, 2006; de Hauteclocque et al., 2012).

The second approach is stochastic: the power density spectrum of the design sea state is used to build long random free surface elevation time-series. The classical approach in wave physics is to use random phases (Zakharov et al., 2012), the amplitudes of each frequency component being defined by the design spectrum. The sequences of free surface elevation are characterized by wave or crest height statistics that depend on the distribution of the random phases.

The duration of the time series is usually equivalent to 3 hours at full scale. Each 3hr-long generated wave sequence is called a "realization" and is sometimes referred to a "run". To evaluate the extreme events occurring with a probability level $P_{\text{design}}$, the total number of waves should be large enough to be statistically reliable. For example, if the chosen criteria impose to ensure the safety of the structures for an event occurring at the probability $P_{\text{design}} = 10^{-3}$, the convergence of the crest height distribution until $P_{\text{design}}$ (evaluated for example using Jeffrey confidence intervals (Brown et al., 2001)) imposes the generation of at least 20 realizations.

In a wave tank configuration, the free surface elevation time-series are generated by a wave maker, whose motion is controlled. Note that the offshore structure model is positioned further in the basin. Therefore, the wave field should be qualified in this area of interest, located at several wavelengths from the wave maker. However, complex nonlinear phenomena such as breaking, or high-order nonlinear wave interactions deeply affect the propagation of the waves (see Sec. 2.2). Consequently, the quantities of interest (spectrum and, crest height distributions) vary from the wave maker to the target position. It is therefore necessary to assess if the wave spectrum generated at the location of interest corresponds to the target design spectrum. Improvements should be considered if the deviations are too great. Moreover, wave statistics should be at least analysed to quantify the severity of the wave field generated.

On those grounds, with a stochastic approach a comprehensive wave qualification procedure relies on the control of i) the measured wave energy spectrum and ii) the wave crest statistics, both at the position of interest in the domain. A procedure is proposed in Det Norske Veritas (2010); NWT Preparation Workgroup (2019); Fouques et al. (2021). It focuses on the control of the spectrum at the target location, through wave maker motion correction processes. Complementary, the wave crest statistics are evaluated using the crest height probability of exceedance (POE). To this aim both the distributions of single realizations (PDSR) and the ensemble distribution (considering all realizations) (PDER) are computed and analysed (Huang and Zhang, 2018). The PDER are compared to the reference distributions (see Sec. 2.1). The present study is based on this wave qualification procedure and the scope is limited to the stochastic approach.

It is worth noting that the procedure presents some limitations. Mainly, the influence of the target location is not taken into account and it relies on the arguable assumption that the generation of the qualified energy spectrum constrains the wave statistics. Numerical studies have led to the observation of configurations exhibiting the same wave energy spectrum but different crest height statistics, depending on the numerical model and the distance from the wave maker (Canard et al., 2020).

In this respect, the aims of the present study are i) to experimentally implement a corrective procedure ensuring the generation of a target spectrum at a specified location of the wave tank, ii) to evaluate the influence of the target location on wave statistics and iii) to study the mechanisms at the origin of the different statistical behaviours that can emerge from a single wave spectrum. The data collected show a significant influence of the target location on the wave statistics, namely kurtosis of free surface elevation as well as crest and height PDER.

This paper is organized into four sections. The first section gives an overview of the physical phenomena that affect the propagation of the waves from the wave maker to the area of interest. It includes the description of theoretical tools developed to characterize and predict the evolution of the stochastic quantities of interest (spectrum and wave statistics). The second section is dedicated to the experimental framework, including details about the geometry, the wave conditions, the wave generation procedure and the experimental uncertainties. Then, the third section summarizes the first step of the experimental study which consists in generating the target wave spectrum at three different locations in the tank. The final section focuses on the statistical properties of the waves depending on the target location.

## 2. Irregular sea state characterization

### *2.1. Reference statistical distributions*

The qualification of the crest PDER relies on comparisons with reference distributions. The shape of the latter depends on the considered spectrum. Over the years, a set of benchmarks has been consecutively developed to account for the different degrees of wave nonlinearities.

At first, the linear prediction was established using the concept of Gaussian wave field, which means that the free surface elevation and its temporal derivation are considered as independent Gaussian random variables. The associated predicted crest distribution is based on the Rayleigh formulation (see Longuet-Higgins (1952)). For a given crest height $H_c$ (height from mean level),

$$P(H_c > \eta) = \exp\left(-8\frac{\eta^2}{H_s^2}\right) \tag{1}$$

$H_s = 4\sigma$ corresponds to the significant wave height and $\sigma$ the standard deviation of the free surface elevation $\eta$. The latter is defined such that its mean value $\bar{\eta}$ is equal to zero.

Nonetheless, the bound waves emerging from second-order nonlinearities are known to break the vertical symmetry of the waves, making the troughs smaller and the crests larger. Theoretical (Tayfun, 1990) and semi-empirical (Forristall, 2000) distributions have been developed to consider those effects. The latter, built with a large number of simulation results, is generally given as a reference by classification societies, see *e.g.* Det Norske Veritas (2010). The mathematical definition follows. For a given crest $H_c$,

$$P(H_c > \eta) = \exp\left(-\left[\frac{\eta}{\alpha_r H_s}\right]^{\beta}\right) \tag{2}$$

For long-crested waves, $\alpha_r = 0.3536 + 0.2892S_1 + 0.106U_r$ and $\beta = 2 - 2.1597S_1 + 0.0956U_r^2$. The Ursell number and the integral steepness are defined as $U_r = \frac{H_s}{k_1^2 h^3}$ and $S_1 = \frac{2\pi}{g}\frac{H_s}{T_1^2}$ with $T_1$ the mean wave period, $k_1$ the corresponding mean wave number obtained from the linear dispersion relation and $h$ the water depth. The mean wave period is defined thanks to spectrum moments ($m_i = \int_0^{f_{\max}} f^i S(f)df$) as $T_1 = m_0/m_1$. $f$ and $S(f)$ respectively stand for the frequency and the energy spectrum. $f_{\max}$ is the highest measured frequency of the wave field.

However, several consecutive studies in wave tank environments found that with high nonlinear wave conditions, the second order references fail to predict the tail of the distributions (Onorato et al., 2006, 2009; Buchner et al., 2011; Latheef and Swan, 2013; Shemer et al., 2010). With no or limited breaking phenomena, the third order nonlinearities appear to strongly increase the number of extreme events, as a result of nonlinear processes such as modulational instabilities or third-order near-resonant interactions. The effects of directionality have also been explored, revealing the limitations of high-order effects for short-crested waves. Note that the conclusions have been established under the assumption of deep water waves, which is the framework of the present study. As a matter of completeness, a reduced water depth is associated with smaller departure from Gaussianity due to third-order effects (Tang and Adcock, 2021). To account for the high-order effects, Huang and Guo (2017); Huang and Zhang (2018) provide a set of semi-empirical crest height benchmark distributions including PDER and PDSR upper and lower bounds. These are assumed to be a realistic statistical description of long-crested wave fields. The distribution is based on a Weibull formulation. The exact definition can be found in Huang and Zhang (2018).

Nevertheless, this distribution was built assuming spatial ergodicity, which is not ensured in a wave tank environment. Its use consequently presents some limitations associated to the spatial evolution of statistical properties detailed in the following section.

### *2.2. Propagation of waves in a wave tank environment*

As mentioned in the Introduction, to develop consistent wave qualification procedures for a wave tank configuration, it is of great importance to account for the physical phenomena that affect the propagation of the waves from the wave maker to the area of interest. This subsection presents an overview of the mechanisms affecting the spectrum and the wave height statistics.

*Evolution of the wave spectrum.* First, the energy spectrum evolves along the wave tank. For deep-water unidirectional nonlinear conditions, third-order wave interactions and more particularly Benjamin Feir instabilities (Benjamin and Feir (1967)) tend to modify the spectrum shape. In order to quantify this phenomenon Janssen (2003) carried out theoretical studies relying on the Zakharov equations as well as the NonLinear Schrödinger (NLS) equations for water waves. The theory mostly predicts a broadening of the wave spectrum along the domain and a downshift of the peak. These phenomena have been observed in a large number of experimental studies Onorato et al. (2006); Shemer et al. (2010); Fadaeiazar et al. (2020).

Furthermore, during the wave propagation in a tank, the wave spectrum is also modified by dissipation mechanisms. Different sources can be identified (Deike et al., 2012). They are due to the effect of viscosity in the: i) fluid bulk, ii) bottom boundary layer, iii) side wall boundary layer, and iv) free surface. In the present study, using a configuration of a deep water towing tank (see Sec. 3.1) and non breaking wave conditions (see Sec. 3.2), the observed dissipation is dominated by viscous phenomena acting on the lateral side walls of the towing tank. A theoretical framework, considering the energy losses of non breaking progressive waves along a tank is described in Kit and Shemer (1989) and Deike et al. (2012). Each Fourier component $A(f, x)$ of the wave field at position $x$ (distance from the wave maker) is expressed as

$$A(f, x) = A(f, 0)\ \exp\left(-\frac{x}{L(f)}\right) \tag{3}$$

with $f$ the frequency of the Fourier component, $A(f, 0)$ the initial Fourier amplitude at frequency $f$, and $L$ the dissipation length, dependent on wave frequency. The latter is defined as,

$$1/L(f) = k\sqrt{\frac{2}{Re}\frac{\sinh(2kh) + kL_y}{\sinh(2kh) + 2kh}} \tag{4}$$

$Re = 2\pi f L_y^2/\nu$ stands for the Reynolds number of the considered frequency component, $\nu$ is the kinematic water viscosity ($\nu = 1.10^{-6}\text{m.s}^2$) and $L_y$ is the wave tank width. Computing the exponential dissipation for all the frequency components, the theoretical wave spectrum $S(f,x)$ at position $x$ is then:

$$S(f,x) = 0.5\,A(f,x)^2/df \tag{5}$$

with $df$ the sampling frequency. The associated significant wave height $H_s(x)$ at position $x$ can be deduced with the spectrum integration over the entire frequency range. Note that those predictions have been established under the assumption of a linear wave field with deep or intermediate water depth.

For extreme sea states, which are not studied in the present paper, the occurrence of breaking events also affects the significant wave height and the spectrum shape, especially for high frequency ranges (Latheef and Swan (2013); Onorato et al. (2006)). However, complex energy cascades limit the accuracy of the predictions (Dommermuth (2021)).

*Evolution of the wave height statistics.* Concomitantly, the spatial evolution of wave height statistics in a wave tank environment is an intricate phenomenon. The wave maker motion is built from a free surface elevation sequence which corresponds to the linear superposition of the input spectrum components with random phases. Therefore, the wave height statistics of this input sequence are Gaussian. However, the generated waves are affected by nonlinearities and as a consequence the statistical properties of the wave field differ from the Gaussian input sequence. The deviations strongly depend on the sea state characteristics and the distance from the wave maker.

With a domain of typical size (propagation length below 60 wavelengths), experimental observations show that the statistical quantities of the wave field vary with the distance from the wave maker (Onorato et al., 2006;

Shemer et al., 2010; Cherneva et al., 2009). This is especially observed for nonlinear narrow-banded spectra. This property of the wavefield can be characterized by the Benjamin Feir Index (BFI), the ratio between the steepness and the nondimensional spectral width, introduced in Janssen (2003). The definition used in the present article was suggested in Serio et al. (2005) as

$$\mathrm{BFI} = \mu_1 \sqrt{2} / \nu_w \tag{6}$$

with $\mu_1 = k_1 \sigma$ the mean steepness and $\nu_w$ the nondimensional spectral width defined with the peakedness method,

$$\nu_w = \frac{1}{Q_p \sqrt{\pi}} \tag{7}$$

with $Q_p = \frac{2}{m_0^2} \displaystyle\int_0^{f_{\max}} f\, S^2(f)\, \mathrm{d}f$. It should be mentioned that this definition of the BFI leads to smaller values that the one used in Onorato et al. (2009) and Onorato et al. (2006), the spectral width being defined in these papers using the half width at the half maximum.

### *2.3. Predictions of the evolution of wave statistics*

Some theoretical tools have been developed over the years to predict the spatial evolution of wave statistics and to quantify the emergence of extreme events, known as rogue waves, along the tank. One of the most relevant approach uses the NLS framework for water waves. Janssen (2003) established an analytical evolution of the wave statistics from a Gaussian to a nonlinear converged wave field. It considers the influence of i) the wave conditions, ii) the water depth and iii) the directionality. The quantity studied is the kurtosis of the free surface elevation, $\lambda_4 = \overline{\eta^4} / \sigma^4$, mainly used to characterize the severity of the wave field. It is found that for unidirectional waves, $\lambda_4$ increases along the tank before reaching a converged value, after a transition area which can reach dozens of wavelengths. The theory has been established under the assumption of deep water waves and narrow banded wave spectra. A complete description can be found in Fedele (2015) and Fedele et al. (2016). Here follows a brief presentation of the main results.

The kurtosis of the free surface elevation can be decomposed into 3 terms,

$$\lambda_4 = 3 + \lambda_{40}^b + \lambda_{40}^d \tag{8}$$

with 3 the Gaussian prediction, $\lambda_{40}^b$ the bound (Stokes) harmonic contribution and $\lambda_{40}^d$ the dynamic component enhanced by nonlinear quasi resonant wave-wave interactions.

$\lambda_{40}^b$ can be directly linked with the vertical asymmetry of the wave field, which is characterized by the skewness of the free surface elevation $\lambda_3 = \overline{\eta^3}/\sigma^3 = \sqrt{\lambda_{40}^b/2}$. The evolution of $\lambda_3$ and $\lambda_{40}^b$ depends on the steepness of the waves. Their asymptotic value can be predicted as $\lambda_3 = 3\mu_1$ and $\lambda_{40}^b = 18\mu_1^2$.

The dynamic excess kurtosis $\lambda_{40}^d$ characterizes the third order nonlinear effects. Its accurate prediction is as a crucial step for the tracking of extreme events. The theoretical framework presented in Janssen (2003); Fedele (2015); Fedele et al. (2016) includes an analytical formula. For unidirectional fields, starting from a Gaussian wave field at the position $x = 0$,

$$\lambda_{40}^d(x) = 6\,\mathrm{BFI}^2\,\Im\left(\int_0^{\nu_w^2\omega_1 x/c_g} \frac{1}{\sqrt{1-2i\alpha+3\alpha^2}}d\alpha\right) \tag{9}$$

with $c_g$ the group velocity at peak frequency and $\omega_1 = 2\pi/T_1$.

Fig. 1 presents $\lambda_{40}^d$ spatial evolution along the ECN towing tank used for the present study (see Sec. 3.1), using the characteristics of the sea state of

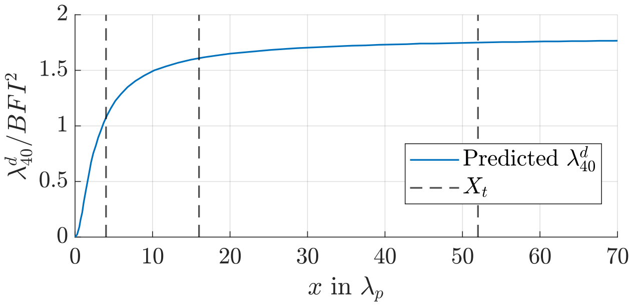

Figure 1: Predicted Excess Kurtosis of the free surface elevation along the tank. Target locations are marked with dotted lines.

interest (see Table 2 in Sec. 3.2). The theoretical excess kurtosis increases monotonically towards an asymptotic value directly linked with the BFI of the wave spectrum,

$$\lambda^d_{40,max} = \mathrm{BFI}^2 \frac{\pi}{\sqrt{3}} \tag{10}$$

The locations of interest $X_t$ of the present study (see Table 2 in Sec. 3.2) are indicated in Fig. 1 with dotted lines. For $X_t = 4\lambda_p$ and $16\lambda_p$, the spatial convergence of the kurtosis is still not reached. Different statistical behaviours are then expected depending on the target position. Note that those predictions do not consider dissipation phenomena.

## 3. Experimental set-up and methods

For the present study, an experimental procedure was implemented, allowing wave generation targeting a design spectrum (whose characteristics can be found in Sec. 3.2) at three positions of the Ecole Centrale de Nantes (ECN) towing tank. This section gives an overview of the set-up and methods

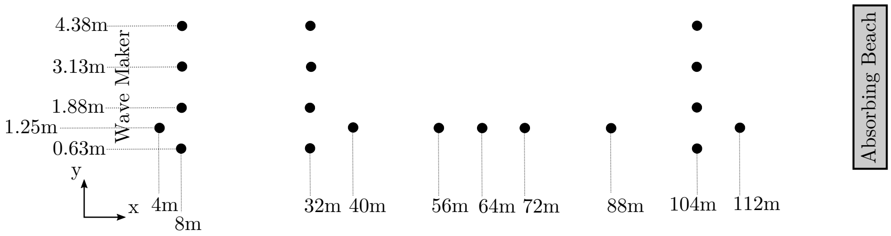

Figure 2: Sketch of the ECN experimental facility with resistive wave probes arrangement (top view).

adopted, including the geometry, the measurement system, the wave conditions, the wave generation procedures and the estimation of the experimental uncertainties.

### *3.1. Experimental set-up*

The experiments were conducted in the ECN towing tank. Figures 2 and 3 present the facility as well as the measurement set-up. The tank is 140m-long and 5m-wide. An absorbing beach beginning at $x_{end} = 134$m limits the reflection. Considering the peak frequency of the generated waves $f_p = 0.88$Hz, the constant depth $h = 2.9$m ensures a dispersion parameter of $k_p h = 9.4$, which is large enough to verify the deep water assumption. The tank is equipped with a monoflap wave maker, with the hinge at 0.47m from the bottom. An optical sensor constantly measures the wave maker motion allowing comparisons with the desired input. Nineteen probes are located all along the domain, allowing an evaluation of the spatial evolution of the wave field see Fig. 3. They consist of resistive gauges measuring the free surface elevation time-series with a 100Hz sampling frequency. The three target positions for the sea state generation are $x = 8$, 32 and 104m from the

Figure 3: Picture of the experimental set-up in the ECN towing tank.

wavemaker. At these locations, four probes are implemented on the plane perpendicular to the propagation direction in order to measure the lateral homogeneity of the wave-field and to identify and quantify the transverse modes excited by the small interstices existing between the lateral vertical walls and the wave maker.

### *3.2. Wave conditions and target locations*

The wave conditions were carefully chosen considering the need for a realistic sea state of use in ocean engineering, which exhibits spatial dynamics, to possibly enlighten the influence of the target location. Breaking conditions were excluded so as to focus on nonlinear effects. Such a wave field is characterized by an intermediate BFI value. As the steepness is limited by the non-breaking condition, a small spectral width must be adopted to increase the BFI. As a result, a moderate steep narrow banded JONSWAP

Table 1: Sea State Characteristics.

| | Experiments | Full scale |
|---|---|---|
| $\gamma$ | 5.0 | 5.0 |
| $H_s$ | 0.05m | 6m |
| $T_p$ | 1.13s | 12.25s |
| $T_1$ | 0.97s | 10.63s |
| $\lambda_p$ | 2m | 234m |
| $\epsilon = \frac{H_s}{\lambda_p}$ | 2.5% | 2.5% |
| $\nu_w$ | 0.144 | 0.144 |
| $BFI$ | 0.51 | 0.51 |

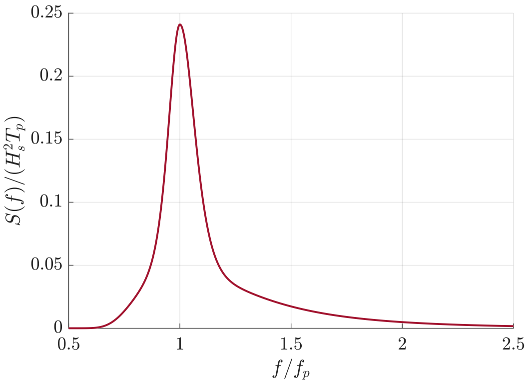

Figure 4: Target wave spectrum.

spectrum was selected (see Komen et al. (1996)). Its shape is defined by

$$S(f) = \frac{\alpha_p g^2}{(2\pi)^4 f^5} \exp\left[-\frac{5}{4}\left(\frac{f}{f_p}\right)^{-4}\right] \gamma^{\exp[-(f-f_p)^2/(2s^2f^2)]} \tag{11}$$

with $f_p$ the peak frequency, $\alpha_p$ the Phillips parameter, $\gamma$ the peak enhancement factor, and $s = 0.07$ for $f < f_p$ and 0.09 for $f > f_p$. The parameters are specified in Table 1 and its shape is presented in Figure 4. Note that wave conditions correspond to a typical "ss6" design sea state (see NWT Preparation Workgroup (2019)) generated at the scale 120, using the Froude similitude. The small frequency bandwidth is ensured by a significant $\gamma = 5$, representative of swell conditions (Det Norske Veritas (2010)). A moderate steepness $\epsilon = \frac{H_s}{\lambda_p} = 2.5\%$ was adopted, which limits the presence of breaking events (Shemer and Alperovich, 2013). The different target positions $X_t$ of the waves generated are listed in Table 2.

Table 2: Target locations.

| $X_t$ (m) | $X_t(\lambda_p)$ |
|---|---|
| 8m | $4\lambda_p$ |
| 32m | $16\lambda_p$ |
| 104m | $52\lambda_p$ |

For the present work the duration of each realization was $900s$ which corresponds to 2h45 at full scale. To consider only fully developed sea state data, the analysis time window was set for each measured time-series to $[x_{max}/c_g(2.2f_p); 900s]$, with $x_{max}$ the position of the last probe and $c_g(f)$ the group velocity at the frequency $f$. The upper limit $2.2f_p$ corresponds to $2H_z$, which is the shortest wave generated due to a mechanical limitation of the wave maker. However, as seen in Fig. 4, the energy content past this frequency is very small. Note that before each run, at least 20min of calm water are ensured to limit the residual waves and currents.

### *3.3. Wave generation*

In order to generate the sea state of interest described in Sec. 3.2, a number of 3-hour full scale realizations were conducted. This section summarizes the procedure used to build each of these runs.

Each realization is associated with a set of input amplitudes $A_{\mathrm{input}}(f_j)$ and phases $\phi_{\mathrm{input}}(f_j)$, related to a free surface elevation time-series $\eta_{\mathrm{input}}(t)$ defined as

$$\eta_{\mathrm{input}}(t) = \sum_{j=0}^{N_{\max}} A_{\mathrm{input}}(f_j) e^{i(2\pi f_j t + \phi_{\mathrm{input}}(f_j))} \tag{12}$$

with $(f_j)_{j\in[1;N_{\max}]}$ the frequencies of the waves to be generated. As mentioned in the Introduction, the phases are random and the amplitudes are built using the input spectrum $S_{\mathrm{input}}(f_j)$,

$$A_{\mathrm{input}}(f_j) = \sqrt{2 S_{\mathrm{input}}(f_j) df} \tag{13}$$

and,

$$\phi_{\mathrm{input}}(f_j) = 2\pi U_{[0;1]} \tag{14}$$

with $U_{[0;1]}$ a random variable following the uniform probability law between 0 and 1. $df$ is the frequency step, chosen for the present study as $df = 1/1024 H_z$. The wave maker transfer function is used to convert $\eta_{\mathrm{input}}(t)$ into wave maker motions. Then, at a position x (distance from the wave maker), the generated free surface elevation $\eta(x,t)$ can be expressed as

$$\eta(x,t) = \sum_{j=0}^{N_{max}} A(f_j, x) e^{i(2\pi f_j t + \phi(f_j, x))} \tag{15}$$

with $A(f_j, x)$ and $\phi(f_j, x)$ the Fourier amplitude and the phase at position $x$ and frequency $f_j$. $\eta(x,t)$ is the quantity measured and analysed. The linear theory predicts $A(f_j, x) = A_{\mathrm{input}}(f_j)$ and $\phi(f_j, x) = -k(f_j)x + \phi_{\mathrm{input}}(f_j)$, with $k(f_j)$ the wave number at frequency $f_j$. However, the nonlinear effects,

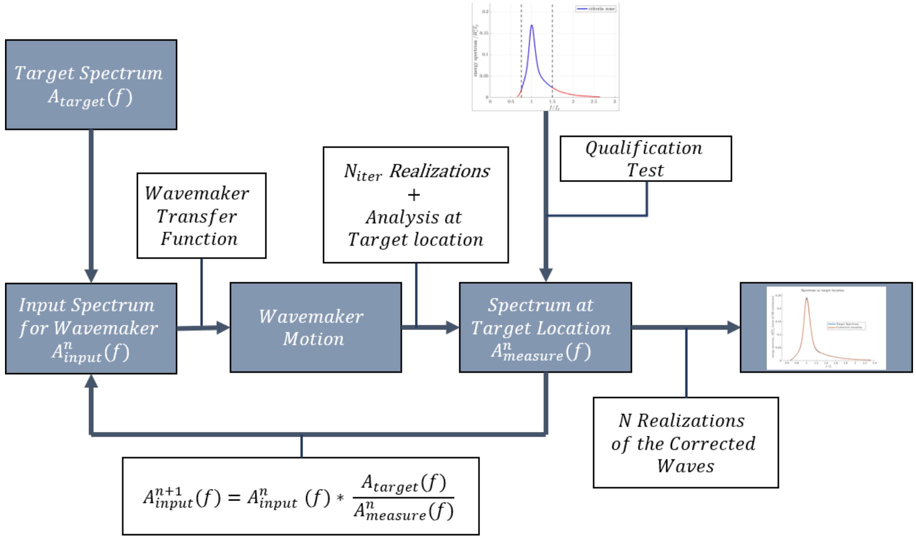

Figure 5: Wave maker motion correction iterative process ensuring the generation of the target spectrum at the location of interest.

the wave maker transfer function uncertainties, the dissipation and the spurious waves result in significant deviations from the linear theory. Therefore, to ensure at the area of interest $A(f_j, X_t) = A_{\text{input}}(f_j)$ the corrective procedure introduced in 3.4 adapts the input amplitudes with a calibration factor $C(f_j, X_t)$,

$$A^{\text{corrected}}_{\text{input}}(f_j) = A_{\text{input}}(f_j)\,.\,C(f_j, X_t) \tag{16}$$

### *3.4. Iterative procedure*

The present study relies on the accurate reproduction of a target wave spectrum at specific locations in the wave tank. Nonetheless, as already mentioned in Sec. 2.2 and 3.3 the spectrum evolves along the tank due to nonlinear wave interactions and dissipation mechanisms. A corrective procedure is needed to ensure the generation of the sea state at a given position. In this respect, the wave maker motion is corrected through a linear iterative process, already successfully tested numerically (Canard et al., 2020) with the open-source wave solver HOS-NWT (Ducrozet et al., 2012). Figure 5 provides a reasonably comprehensive overview of the procedure used to control the quality of the wave field generation in the experimental wave tank.

The first series of runs use the target spectrum as input for the wave maker motion. Then, the Fourier amplitudes are iteratively corrected using the spectrum measured at the target location $X_t$. At iteration $n+1$, each input amplitude $A_{input}^{n+1}(f)$ is expressed as

$$A_{input}^{n+1}(f) = A_{input}^{n} \frac{A_{target}(f)}{A_{measure}^{n}(f)} \tag{17}$$

with $A_{target}(f)$ and $A_{measure}^{n}(f)$ the Fourier amplitude of the target and measured spectrum at iteration n. Note that for the present study each iteration test consists of six realizations. $A_{measure}^{n}(f)$ is built using the spectrum $S_{measure}^{n}(f)$ obtained at $X_t$ and averaged over the six realizations. This ensures a large enough number of waves to obtain converged Fourier amplitudes. The estimation of the spectra is performed with the Welch method applied on the measured free surface elevation time series, using time windows of approximately $50T_p$ (Welch, 1967).

The process ends when the spectrum measured at the target location matches the target sea state. Verification is performed using the wave qualification criterion detailed in NWT Preparation Workgroup (2019) and Canard et al. (2020). It evaluates the difference between the target and the measured spectra. The deviation must be within $C = 10\%$ for frequencies in the range $f \in \left[\frac{3}{4}f_p; \frac{3}{2}f_p\right]$ with $f_p$ the peak frequency of the corresponding spectrum. The significant wave height is also used to qualify the wave field. Deviations below 5% are accepted. Note that the typical wave qualification criteria used in numerical frameworks are more restrictive (Det Norske Veritas, 2010; NWT Preparation Workgroup, 2019; Canard et al., 2020). Indeed spurious events such as reflection or transverse modes together with measurement uncertainties alter the efficiency of the process. After convergence of the spectrum, 30 realizations of the corrected sea states are generated. The results presented in Sec. 4.2 and 5 use the corresponding 17,000 waves at peak period (considering the analysis time window). The procedure is repeated for the three target locations (Tab. 2).

### *3.5. Uncertainties*

Particular attention was paid to the measurement and generation uncertainties during the experimental campaign. The quality of the results is mainly affected by i) the reliability of the measurement system (wave gauge uncertainties), ii) the mechanical defects affecting the generation (wave maker transfer function uncertainties), and iii) spurious waves affecting the propagation (transverse modes, reflection, residual waves present when launching a run). Note that the relevance of the measured stochastic quantities of interest is also challenged by a statistical reliability. The method adopted for the present study considered only the the most critical uncertainties. First, uncertainty ranges were estimated, taking into account i) wave gauge uncertainties, ii) repeatability issues and iii) statistical reliability. Then the influence of spurious waves (reflection and transverse modes) was examined.

*Uncertainty ranges.* The reliability of resistive wave gauges was explored throughout the experimental campaign. These sensors, which rely on water conductivity, are very sensitive to temperature, resulting in significant changes in the calibration factors during experiments lasting for several days/weeks. Repeatability tests were therefore performed at least once a day to monitor the quality of the measurements. These dedicated experiments were used to adapt the calibration factors of the wave gauges daily. A calibration bench was also used to re-calibrate the gauges in the event of strong variations.

The influence of these corrections was quantified to compute uncertainty ranges. A brief description of the method follows. For each probe, the measured free surface elevation was computed as

$$\eta_{\mathrm{WG}}(t) = U(t)\, G_{\mathrm{WG}} \tag{18}$$

and,

$$G_{\mathrm{WG}} = G_{\mathrm{WG}}^{B}\, C_R \tag{19}$$

with $t$ the time, $U$ the voltage given by the measurement acquisition system, $G_{\mathrm{WG}}$ the corrected calibration factor, $G_{\mathrm{WG}}^{B}$ the calibration factor in meters per volt obtained from the calibration bench and $C_R$ the non-dimensional correction factor estimated from repeatability tests. $G_{\mathrm{WG}}^{B}$ and $C_R$ were kept constant during a run. Then, the uncertainties of the corrected calibration factor $\delta G_{\mathrm{WG}}$ can be quantified as

$$\frac{\delta G_{\mathrm{WG}}}{G_{\mathrm{WG}}} = \sqrt{\left(\frac{\delta G_{\mathrm{WG}}^{B}}{G_{\mathrm{WG}}^{B}}\right)^2 + \left(\frac{\delta C_R}{C_R}\right)^2} \approx 2.5\% \tag{20}$$

Besides, variations in the quantities of interest ($H_s$ and spectrum) were observed by comparing several repeatability runs generated the same day. The associated standard deviations of the $H_s$ was 1%. Considering the short duration between these runs, the deviations of the wave gauge calibration factors cannot explain the variations observed. The former are likely to come from the residual waves and currents (van Essen and Lafeber, 2017) that are still present at the beginning of the runs and the unavoidable perturbations of the measurement acquisition system.

Lastly, it should be remembered that the $H_s$ and the wave spectra presented in this article are mean stochastic quantities, averaged over several realizations. Consequently, the sampling variability (i.e. the statistical uncertainties) limits the accuracy of the results. This can be quantified through the use of the standard deviations of the quantities of interest over all the realizations. Note that the former also includes the effects of the repeatabilitiy issues previously described.

Then, considering wave gauge uncertainties and grouping the influence of repeatability and statistical issues by the use of the standard deviations over all the realizations, the total uncertainties of the mean $H_s$ and spectrum can be estimated as

$$\frac{\delta H_s}{H_s} = \frac{1}{H_s} \frac{\sigma_{real}^{H_s}}{\sqrt{N_{real}}} + \frac{\delta G_{WG}}{G_{WG}} \tag{21}$$

$$\frac{\delta S(f)}{S(f)} = \frac{1}{S(f)} \frac{\sigma_{real}^{S(f)}}{\sqrt{N_{real}}} + 2\frac{\delta G_{WG}}{G_{WG}} \tag{22}$$

with $\sigma_{real}^{X}$ the standard deviations of a stochastic quantity $X$ over all the realizations and $N_{real}$ the number of realizations. Note that $\delta H_s/H_s \leq 3.5\%$

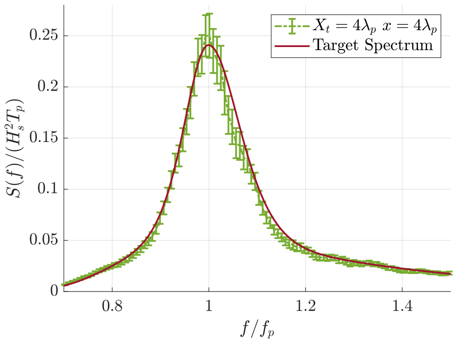

Figure 6: Mean spectrum and associated uncertainty ranges (at the target location after the iterative correction procedure described in Sec. 3.4)

and $\delta S(f)/S(f) \leq 6\%$ for the following results obtained with 30 realizations of a 3-hour full scale sea state. As an example, Figure 6 displays the uncertainty ranges for the mean spectrum measured at $x = 4\lambda_p$ after the iterative correction procedure described in section 3.4. The magnitude of the wave spectrum uncertainties are always similar to the ones presented here. For the sake of clarity, in the next sections that involve comparisons of different spectra, uncertainty ranges will only be displayed for the significant wave height.

The non-dimensional quantities, such as the kurtosis of the free surface elevation or the normalized crest height distributions, are not influenced by uncertainties in the wave gauge calibration factors. Nonetheless, their quality is affected by the sampling variability which depends on the size of the data-set (Bitner-Gregersen et al., 2020). As for the spectrum and the significant wave height, the statistical uncertainties of the kurtosis were evaluated through the use of its standard deviation over the realizations,

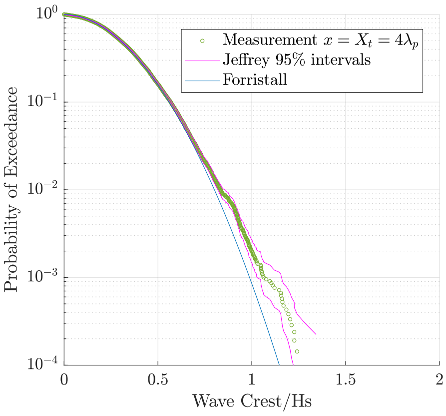

Figure 7: Crest height PDER and associated Jeffrey intervals (at the target location after the iterative correction procedure described in Sec. 3.4)

$$\delta\lambda_4 = \sigma_{real}^{\lambda_4}/\sqrt{N_{real}} \tag{23}$$

For the PDER, the sampling variability can be estimated by computing 95% Jeffrey confidence intervals (Brown et al., 2001). As an example, Figure 7 presents the crest height PDER at $x = 4\lambda_p$ after the iterative correction of the spectrum, gathering data from 30 realizations. The associated 95% Jeffrey intervals are displayed in pink. The uncertainties are relatively greater for the smallest probability of occurrence. Note that the confidence intervals depend only on the length of the data-set. Hence, their magnitude does not vary significantly among the configurations analysed in the present article. On these grounds, in the following sections, only the probabilities greater than $10^{-3}$ will be considered. This limits the relative errors on the wave crest height to approximately 5%. For the sake of clarity, the Jeffrey intervals will not be displayed in the following sections where different PDER are compared.

*Spurious Waves.* Reflection is limited by the absorbing beach located at the end of the experimental wave tank. Its performance has been assessed by an analysis of the remaining waves after the runs and using experimental studies in regular waves estimating the efficiency of the absorbing beach for frequencies close to the peak frequency of the spectrum. The amount of reflection was estimated to 5% of the incident wave height. Note that it was checked thanks to numerical simulations that this amount of reflection has no influence on the results presented hereafter (spectrum, kurtosis, PDER, groupiness factors).

Transverse modes, excited by the gaps between the wave maker and the side walls were also observed. In particular, modes 2, 4 and 5 were identified. To reduce their influence, the positions of the four gauges installed at each area of interest were carefully chosen to be on Mode 4 nodes (see Fig.2). As shown in Figure 8, with such a set-up, the sum of the amplitudes of the identified modes at measurement points vanished. Then, when taking the average of the 4 free-surface elevation time series, the lateral symmetry of the flow erases the influence of modes 5 and 2. Noise analysis after the runs showed that the amplitudes of the transverse modes are limited to 5% of the generated wave field.

## 4. Controlled irregular wave generation

This section presents the first step of the experimental study, which consists in generating the sea state characterized in Tab.1 at three locations in

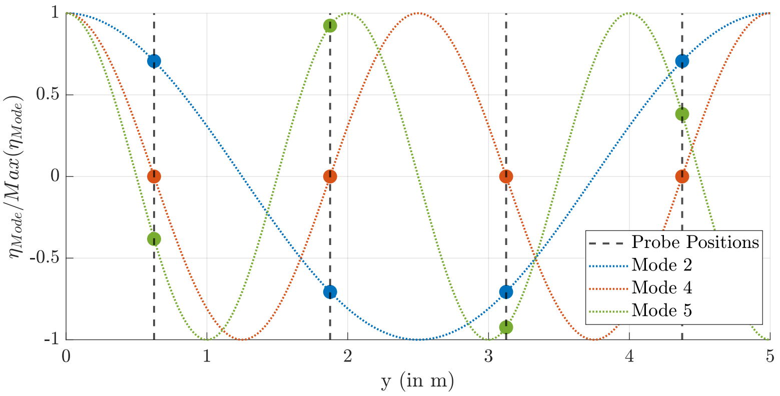

Figure 8: Outline of the identified transverse modes along a transverse line in the tank. Amplitudes of the modes at measurement points are marked with circles

the wave tank. First, the need for a correction procedure is demonstrated. Then, the chosen iterative procedure is applied and the corresponding results provided.

### *4.1. Wave propagation in the tank*

The sea state described in Sec. 3.2 was created in the ECN towing tank using the first step of the generation procedure (see Sec. 3.3). Ten 900s-realizations were generated, without any correction applied to the input spectrum. The corresponding analysed data contained 5,500 waves at peak period per wave gauge. This ensures the statistical convergence of the wave spectra obtained.

Figure 9 presents the spatial evolution of $H_s$ along the tank. As expected, the wave field is characterized by the target significant wave height at the wave maker location. This is followed by a 10% decrease of $H_s$ over the long-distance (around $54\lambda_p$) propagation in the experimental tank. Note that

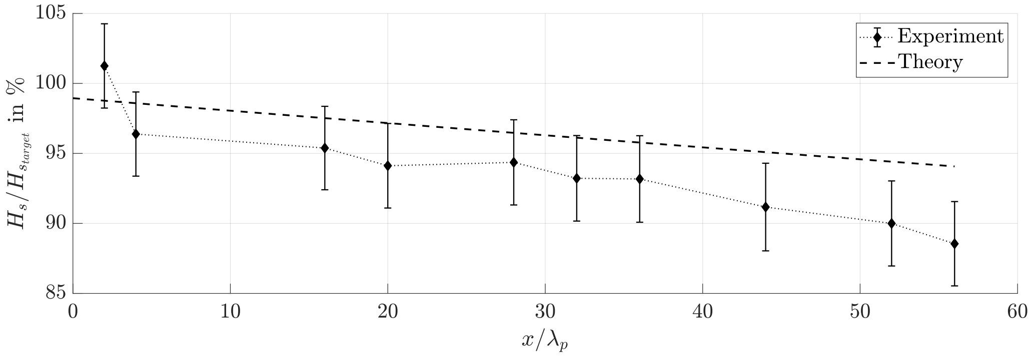

Figure 9: $H_s$ along the tank without correction of the wave maker motion

no breaking events were observed. Therefore, the dissipation is likely to be dominated by viscous phenomena acting on the lateral side walls of the tank.

The linear predictions presented in Sec. 2.2 for the spatial evolution of the significant wave height along the tank have been included in Fig. 9. In view of the uncertainty ranges, the dissipation theory slightly underestimates the decrease of $H_s$, especially at the end of the tank. This behaviour of the model was also observed in Deike et al. (2012) focusing on regular wave cases. The differences with the experimental results were explained by the effects of viscosity over the free surface, which are not taken into account in the theory. In the present study, where nonlinear irregular wave fields were observed, the inaccuracy of the predictions can also be due to nonlinear mechanisms.

Concomitantly, Figure 10 presents the spectrum at $x = 4$, 16 and $52\lambda_p$, giving an overview of the spectrum evolution along the tank. As expected, close to the wave maker ($x = 4\lambda_p$) the spectrum lies almost exactly on the target shape. Then, as the distance from the wave maker increases, energy

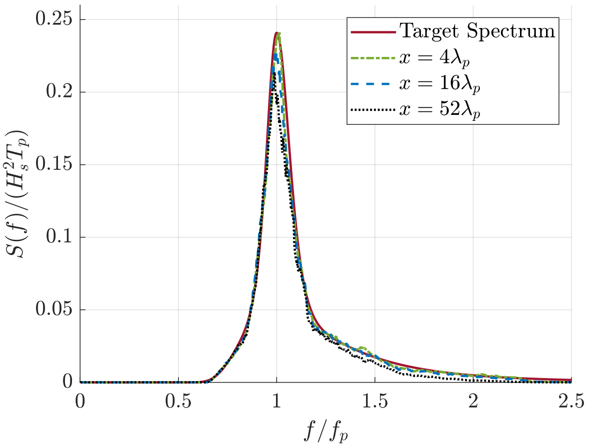

Figure 10: Spectrum along the tank without correction of the wave maker motion

dissipation significantly affects the peak and the tail of the spectrum (respectively $f/f_p \in [0.95; 1.05]$ and $f/f_p \geq 1.2$). As mentioned in Sec. 2.2, a broadening of the spectrum along the tank is predicted, due to nonlinear wave interactions (see Janssen (2003)). However, this phenomenon was not observed here. Dissipation mechanisms seem to counterbalance the broadening.

The spectrum is not qualified in most parts of the tank. For the present study, we tolerate $H_s$ and spectrum shape deviations up to 5 and 10% respectively. This is clearly not satisfied here for $x \geq 16\lambda_p$. Therefore, the corrective procedure introduced in Sec. 3.4 is needed to ensure the generation of the target sea state at any specified location in the tank.

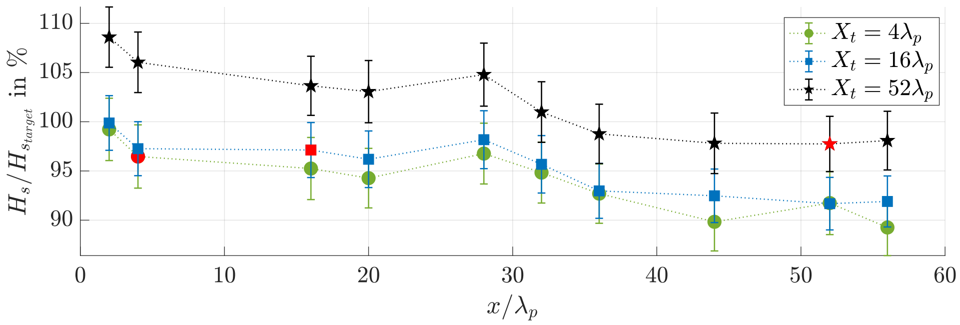

Figure 11: Significant wave height along the tank. Target locations are marked in red.

### 4.2. Results after correction

Then, using the corrective procedure introduced in Sec. 3.4, three wave series were successfully generated, after 2, 3 and 3 iterations for $X_t = 4\lambda_p$, $16\lambda_p$, and $52\lambda_p$ respectively. This means that at the location of interest, the target spectrum was measured within the accuracy range of 10%. Note that hereafter, converged wave series will refer to a set of realizations generated with the corrective procedure. Each series is then associated with a target location $X_t$.

Figure 11 presents the spatial evolution of $H_s$ along the tank for the three converged series. As already observed for the waves generated without the correction (Fig. 9) $H_s$ decreases significantly during wave propagation. However, the corrective procedure ensures a value close to the target $H_s$ ($H_{s_{target}}$) near the positions of interest. It compensates the energy losses with an increased energy level delivered by the wave maker, dependent on the target location.

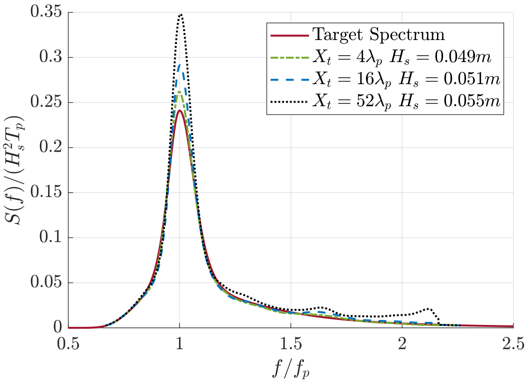

Figure 12: Input spectrum for each wave series.

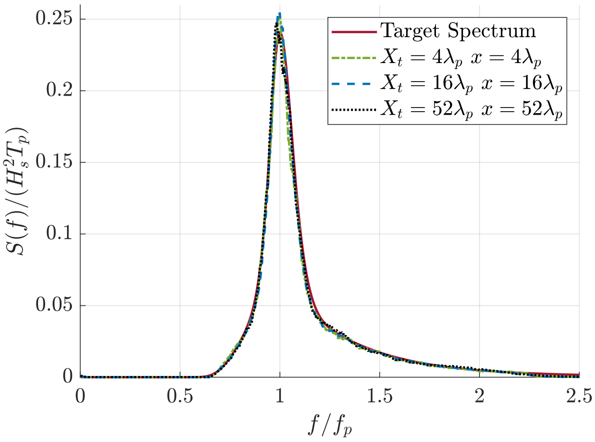

Figure 13: Energy wave spectrum at target location for the three generated wave series.

Table 3: Spectrum Parameters at Target Locations.

| $X_t$ | $4\lambda_p$ | $16\lambda_p$ | $52\lambda_p$ |
|---|---|---|---|
| $H_s$ (% $H_{s_{\text{target}}}$) | 97 | 97 | 98 |
| $T_1$ (% $T_{1_{\text{target}}}$) | 103 | 103 | 103 |
| $\nu_w$ | 0.136 | 0.132 | 0.135 |

Figure 12 presents the converged wave maker input spectra. As can be seen in Fig. 11, the significant wave height of the input spectrum increases with $X_t$ to ensure $H_s \approx H_{s_{target}}$ at $x = X_t$. As expected from dissipation observations in Fig. 10, the energy added by the corrective procedure is mainly located around the peak frequency and in the high frequency domain. Note that the above-mentioned mechanical limitation of the wave maker motions at $f = 2Hz = 2.2f_p$ is clearly seen. The procedure also induces a slight increase in the input spectra BFI with $X_t$: BFI = 0.50, 0.54 and 0.61 for $X_t = 4\lambda_p$, $16\lambda_p$ and $52\lambda_p$ respectively.

As the final result of the iterative procedure, Fig. 13 presents the converged spectrum at the three target locations. The deviations from the target sea state observed in Fig. 10 have all been corrected. The corrective procedure ensures the generation of a converged spectrum lying on the target shape (with a 10% tolerance). Table 3 presents the main parameters of the spectrum at the target location. The values are almost independent of the target location.

The first objective of the present study has therefore been achieved, i.e., the target sea state can be accurately generated anywhere in the tank. The corrective iterative procedure, already numerically tested and validated (see

Canard et al. (2020)) has been successfully implemented in an experimental configuration that is more complex than the one used in the numerical simulation due to the dissipation and the measurement uncertainties. From this point, it is of great importance to remember that for each converged series the target spectrum is accurately controlled at its target location.

## 5. Wave Statistics at different locations

The sea state described in Tab. 2 was successfully generated in the ECN towing tank at consecutively $4\lambda_p$, $16\lambda_p$ and $52\lambda_p$ from the wave maker. This section presents the second step of the experimental study, which consists in comparing the statistical characteristics of the converged series depending on the target location.

### *5.1. Higher order statistics: kurtosis*

The first quantity of interest is the kurtosis of the free surface elevation $\lambda_4$, commonly used to easily estimate the probability of occurrence of extreme waves (see for example Kirezci et al. (2021); Annenkov and Shrira (2009); Christou and Ewans (2014)). As a reference, $\lambda_4 = 3$ corresponds to the Gaussian wave fields (i.e. linear superposition of independent frequency components). However, the nonlinear effects are known to increase the kurtosis values (see Sec. 2.2 and 2.3).

The measured $\lambda_4$ evolution along the experimental wave tank is presented in Fig. 14 . The red line corresponds to the theoretical results predicted by the theory described in Sec. 2.3. As expected, for the three converged series the kurtosis is around 3 near the wave maker (signature of the imposed Gaussian wavefield) before increasing along the tank. The observed order of

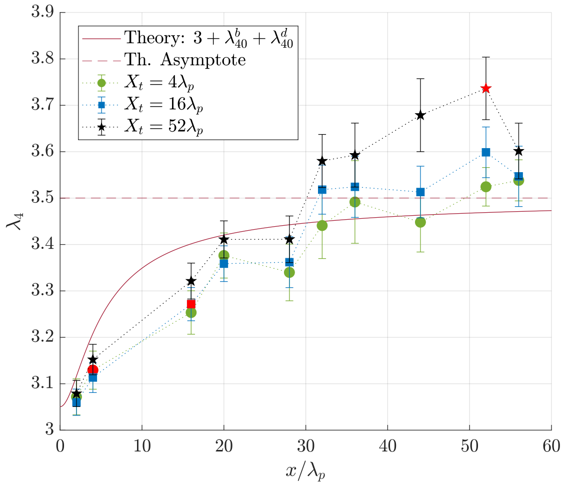

Figure 14: Kurtosis of the free surface elevation along the tank. Target locations are marked in red.

magnitude corresponds to the theoretical prediction. As a consequence, the four-wave near-resonant interactions considered in the latter are likely to be at the origin of the measured increase in kurtosis. No significant changes of behaviour were observed when changing the target location $X_t$. Note that a larger $X_t$ leads to larger values of kurtosis at a given position. This observation can be explained by the properties of the converged input spectra, the initial BFI of the latter being slightly larger for larger $X_t$ (see Sec. 4.2). At the end of the domain ($x > 30\lambda_p$), the value of the kurtosis stabilises in agreement with the theoretical predictions.

The target locations are colored in red in Fig. 14. The same spectrum generated at $X_t = 4\lambda_p$, $16\lambda_p$ and $52\lambda_p$ is associated with kurtosis of 3.1, 3.3 and 3.7 respectively. The different kurtosis values observed at $X_t$ depending on the converged series demonstrate that a single wave spectrum can be associated with clearly different statistical behaviours. The influence of the spectrum corrective process is significant only for the spectrum shape, and does not deeply interfere with the nonlinear mechanisms responsible for the kurtosis increase along the tank (Fig. 14). Consequently, the target spectrum can be easily generated at a specified location but its associated kurtosis (or equivalently probability of occurrence of large waves) is strongly dependent on the distance from the wave maker. While the theory is an interesting framework to easily obtain a first estimate of the kurtosis dependence on $X_t$, these predictions assume narrow banded weakly nonlinear waves and do not account for the spectrum evolution along the tank; which limits the scope of applications.

### *5.2. Wave crest probability of exceedance*

As mentioned in the Introduction, the ensemble distribution considering all the realizations (PDER) is a crucial quantity, typically used in industry as the statistical quantity of interest for wave qualification procedures (see Det Norske Veritas (2010)). The study of the PDER allows for a fine analysis of the occurrence of extreme events . The kurtosis, characterizing the whole tail of the PDER, is less accurate in this context.

Figure 15 presents the crest PDER at $x = X_t$ for the three converged series. As a reminder, the associated wave spectra are identical (see Fig. 13). The Forristall and Huang references were built using the target spectral parameters. Each distribution is non dimensional and expressed with respect to the measured significant wave height. Note that with the number of waves used to build the distributions, the probabilities below $10^{-3}$ are not

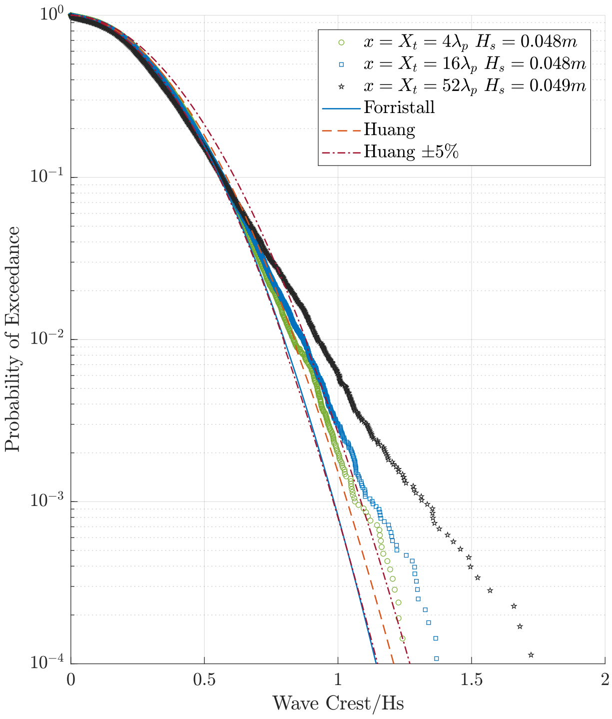

Figure 15: Ensemble crest distribution at target location for the three wave series generated.

statistically converged and should not be analysed (see section 3.5).

First, Fig. 15 should be related to the red markers in Fig. 14 which correspond to the kurtosis at $X_t$ for the three converged series. In the previous subsection, we observed that the free surface elevation statistics evolve along the tank and that this evolution is almost independent of the target location. As a consequence, the same spectrum was associated with various values of kurtosis, depending on $X_t$. The study of the PDER clearly exhibits the same trend. For a single qualified spectrum, the target position strongly affects the tail of the crest PDER, the occurrence of extreme events increasing with $X_t$. As a result, the probability of exceedance $POE = 10^{-3}$ is associated with the normalized crest height $H_c/H_s = 1.06$, 1.13 and 1.31 for $X_t = 4\lambda_p$, $16\lambda_p$ and $52\lambda_p$ respectively. Note that the definition of rogue waves proposed in Haver (2001) corresponds to $H_c/H_s > 1.25$, which is associated far from the wave maker with quite a large probability of occurrence.

Moreover, for this sea state exhibiting intermediate BFI=0.51, the Forristall distribution is not relevant, even in the areas close to the wave maker. The Huang distribution, built to capture the high order nonlinear effects also fail to predict the tail of the distribution for $X_t > 4\lambda_p$. When generating long-crested sea states in a wave tank facility, both those reference distributions can significantly underestimate the largest waves appearing in a sea state. This has a possible significant impact on the design of model tests in ocean engineering.

Attention should therefore be paid to the usual wave qualification procedures used in industry. The latter consist in targeting a wave spectrum at a given position and then comparing it with the benchmark distributions.

Nonetheless, the data yielded by this study show that in the case of moderate BFI unidirectional sea states, the benchmark distributions are not relevant and depending on the target location, the crest statistics are different even if the target spectrum is qualified.

### *5.3. Distributions of wave heights and wave periods*

In order to investigate the characteristics of the extreme events appearing for the largest $X_t$, the present subsection focuses on the distributions of the wave heights and periods. To compute the crest height distributions presented in the previous section, the free surface elevation time series are divided into sequences of zero-crossing waves. Each of the identified events is characterised by a crest height $H_c$, a wave height $H$ and a wave period $T$ (see Fig. 16).

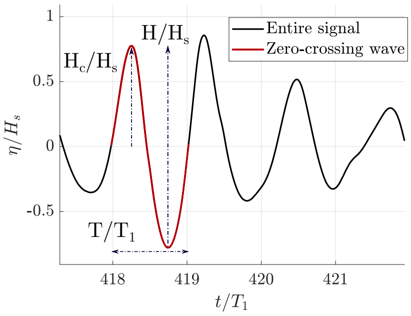

Figure 16: Definition of zero crossing wave parameters.

Then, complementary to Fig. 15 presenting the crest height PDER for the three converged series, Fig 17 presents the wave height and the wave period ensemble distributions. As expected, the shape of the wave height PDER depends on the target location. For the more extreme events ($POE < 10^{-2}$), at a given probability level the heights of the zero crossing waves increase with $X_t$. As an example, the probability of exceedance $POE = 10^{-3}$ is associated with the normalized wave height $H/H_s = 1.8$, 1.9 and 2.2 for $X_t = 4\lambda_p$, $16\lambda_p$ and $52\lambda_p$ respectively. Note that one of the usual definition of a rogue wave is $H/H_s > 2$ (see Onorato et al. (2013)), a threshold which is reached for $X_t = 52\lambda_p$. This corroborates the analysis of the crest height PDER presented in the previous section. However, the target location does not affect the wave period PDER. For the three converged series, the distributions are nearly identical, which means that the period of the extreme events does not depend on the distance from the wave maker, even if their crest and wave height increases with $X_t$.

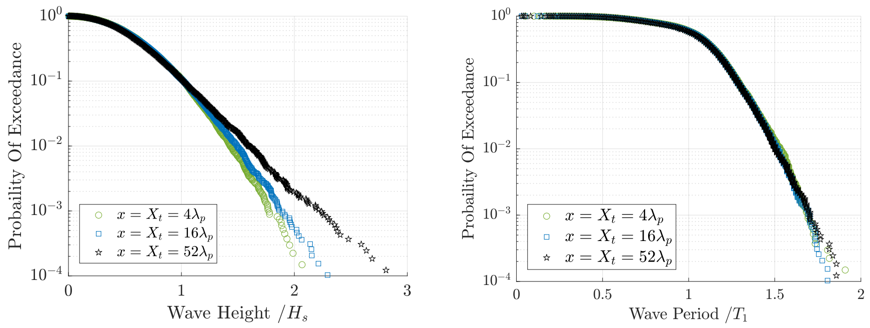

Figure 17: Ensemble wave height distribution (left) and Ensemble wave period distribution (right), at target location for the three wave series generated.

To complete the analysis, Fig. 18 presents the joint probability density function of wave heights and periods for the three converged series. First, we clearly observe that regardless of the target location, the most probable events are located around the point ($H = 0.7H_s$, $T = 1.1T_1$). This is in agreement with the PDER presented in Fig 15 and 17, in which only the tail of the wave and crest height distributions are affected by $X_t$. Then, the events characterised by $H > 1.1H_s$, exhibiting different probabilities of exceedance in Fig. 17 are all located in Fig. 18 between $T/T_1 = 0.8$ and $T/T_1 = 1.3$. Their probability of occurrence obviously increases with $X_t$ (spreading of the probability density function towards the largest wave height). Therefore, when targeting a spectrum at a specified location in a wave tank, the occurrence of extreme events increases with $X_t$. These events are characterised by large wave heights with similar wave periods whatever the propagating distance. In other words, the periods of the extreme waves are not extreme. They stand close to $T_1$, which corresponds to the period of the most probable events. Only the height of the extreme events increases with $X_t$. This increase is a consequence of the nonlinear effects described in Sec. 2.2 and can't be predicted with a linear approach (see Forristall (2017)). In a wave tank environment, an accurate representation of the joint wave height and period statistics should account for the distance from the wave maker, even if the period distributions stand linear independently of $X_t$.

### *5.4. Wave Envelope characteristics*

In the previous subsections we showed that depending on the target location, the qualified spectrum is associated with significantly different wave statistics (kurtosis, crest and wave height distributions). The features of the wave envelope are here studied to characterize in greater details the influence of the target location on the wave field properties.

The properties of the envelope of ocean waves and in particular its asso-

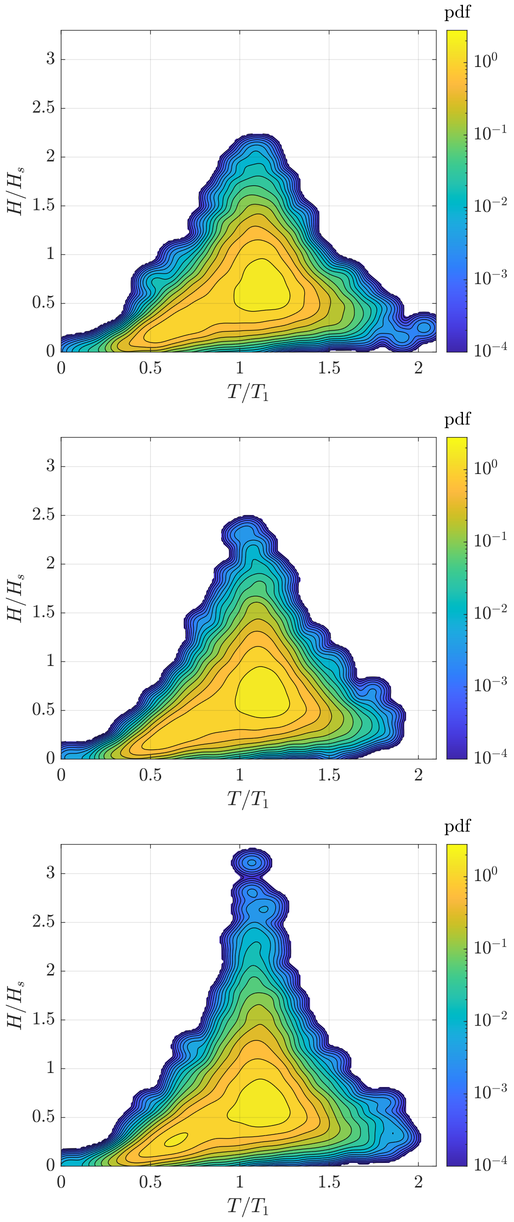

Figure 18: Ensemble joint probability density function of zero crossing wave heights and periods, for $x = X_t = 4\lambda_p$ (top), $x = X_t = 16\lambda_p$ (middle), $x = X_t = 52\lambda_p$ (bottom).

ciated wave groups have been extensively studied over the past years, as they have a significant role in coastal and offshore engineering (Mase, 1989; List, 1991; Haller and Dalrymple, 1995; Saulnier et al., 2011; Huang and Dong, 2021). A wave group is usually defined as a sequence of waves over a given threshold. Its properties are known to have a strong influence on offshore structures' stability, wave breaking, and the number of extreme events in the wave field (Huang and Dong, 2021). To account for the number and the severity of the wave groups in a given wave field, the notion of groupiness has been established. A set of groupiness factors (GF) can be defined (Haller and Dalrymple, 1995; Huang and Guo, 2017), the main idea being to quantify the intensity of the wave groups through the use of the standard deviation of the envelope or the instantaneous energy of the wave field. Here follows a brief description of the two groupiness factors computed for the present study. More detailed definitions and characteristics of those quantities can be found in Huang and Dong (2021).

The first definition relies on the wave envelope estimation. The envelope $\Psi(t)$ is computed through the use of the Hilbert transform $\hat{\eta}(t)$ of the free surface elevation time series (Hudspeth and Medina (1989)).

$$\Psi(t) = |\eta(t) + i\hat{\eta}(t)| \tag{24}$$

Then, the groupiness factor is computed as

$$\mathrm{GF} = \frac{\sqrt{2}\sigma_\Psi}{\overline{\Psi}} \tag{25}$$

with $\overline{\Psi}$ and $\sigma_\Psi$ the mean and the standard deviation of the wave envelope.

Through the use of the smoothed instantaneous wave energy history approach (hereafter SIWEH), another definition of the groupiness factor was

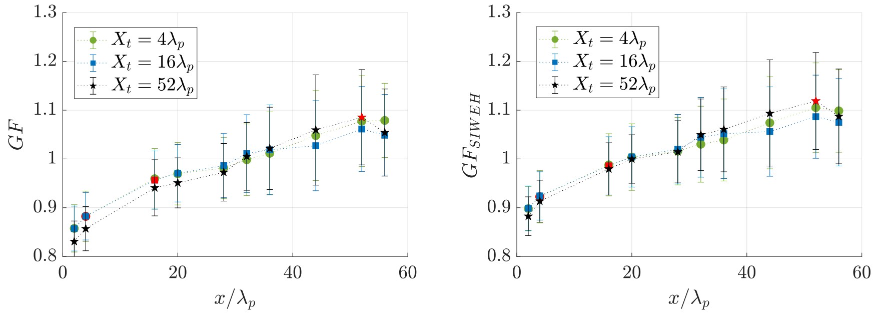

Figure 19: Groupiness factor computed with the envelope method (left) and SIWEH method (right). Target locations are marked in red.

established in Funke and Mansard (1980). The procedure relies on the computation of the instantaneous wave energy

$$E_S(t) = \frac{1}{T_p} \int_{-\infty}^{+\infty} \eta^2(t)(t+\xi)Q(\xi)d\xi \tag{26}$$

with

$$Q(\xi) = \begin{cases} 1 - |\xi/T_p| & \text{if } \xi \in [-T_p, T_p] \\ 0 & \text{otherwise.} \end{cases} \tag{27}$$

Similarly to the envelope method, the groupiness factor is then obtained by computing the standard deviation of $E_S(t)$.

$$\mathrm{GF}_{\mathrm{SIWEH}} = \frac{1}{\overline{E_S(t)}} \sqrt{\frac{1}{T_{end} - T_{beg}} \int_{T_{beg}}^{T_{end}} (E_S(t) - \overline{E_S(t)})^2 dt} \tag{28}$$

with $T_{beg}$ and $T_{end}$ defining the time window analysis of the considered free surface elevation time series. The groupiness factors GF and $\mathrm{GF}_{\mathrm{SIWEH}}$ were computed for each realization and for each wave gauge.

Figure 19 present the GF and $\mathrm{GF}_{\mathrm{SIWEH}}$ along the tank for the three experiments. The presented quantities are the means of all the realizations.

Uncertainty ranges correspond to the associated standard deviations. Lastly, note that the target locations are marked in red. Obviously, the two different groupiness factors lead to similar results, the values of $\mathrm{GF}_{\mathrm{SIWEH}}$ being slightly larger than GF values. On the two figures, for each converged series, GF increases along the tank which means that large and clear-cut wave groups appear as the waves propagate. This increase can be directly correlated with the kurtosis evolution (see Sec. 5.1). The enhanced occurrence of extreme waves with propagating distance is associated with the increased existence of wave groups. Note that these results should be compared with another experimental study carried out in the ECN towing tank (see Michel et al. (2020)). In the latter, the evolution of regular waves slowly modulated in amplitude and phase was associated with the emergence of coherent structures (Peregrine solitons) during the propagation, as a direct result of near-resonant wave interactions (self-focusing). This phenomenon appears to be strongly related to the spatial kurtosis evolution and is likely to be connected to the GF increase measured in the present study.

The influence of the corrective process is once again limited. The evolution of the groupiness factors does not depend on the input spectrum variations that correct the spectrum at target location. Therefore, for each converged wave series, the groupiness factors are mainly dependent on the distance from the wave maker, the wave groups being more defined at the end of the tank. Hence, a single wave spectrum can be associated with wave fields characterised by different groupiness.

Figure 20 illustrates the influence of the target location on the wave groupiness. It presents typical free surface elevation time series at $x = X_t$ for

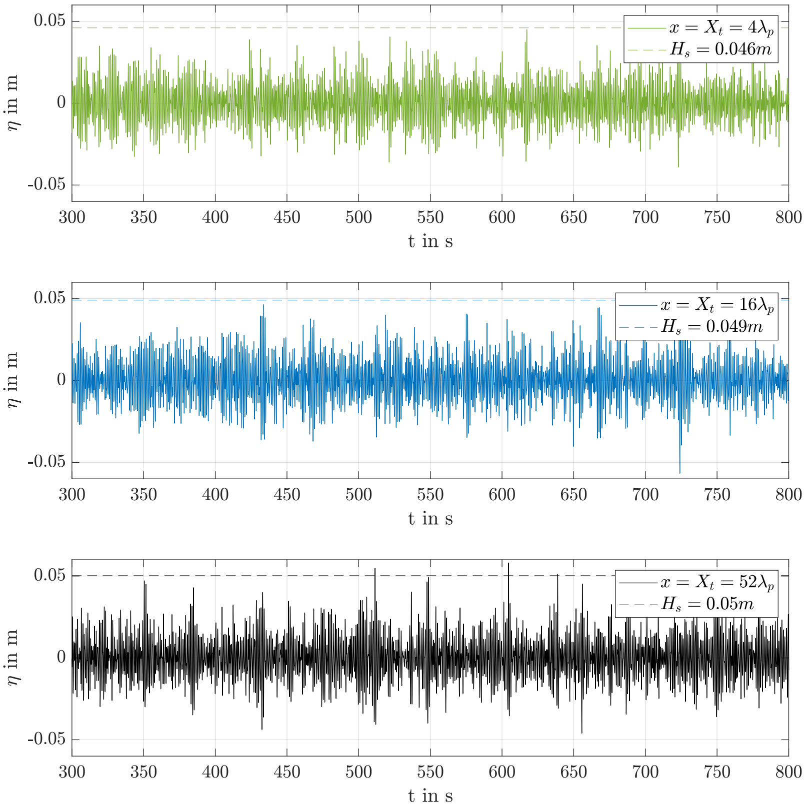

Figure 20: Typical free surface elevation time series extracted from the 3 converged series. Local $H_s$ values are indicated with dotted lines.

Table 4: Mean Parameters at Target Locations.

| $X_t$ ($\lambda_p$) | 4 | 16 | 52 |
|---|---|---|---|
| $GF$ | 0.89 | 0.96 | 1.09 |
| $GF_{SIWEH}$ | 0.92 | 0.99 | 1.12 |
| $\lambda_4$ | 3.1 | 3.3 | 3.7 |
| $H_c/H_s$ for $POE = 10^{-3}$ | 1.06 | 1.13 | 1.31 |
| $H/H_s$ for $POE = 10^{-3}$ | 1.8 | 1.9 | 2.2 |

the three converged series. Visually, the wave groups are more clear-cut for the larger $X_t$. Concomitantly, it results in a larger number of extreme events. Indeed, the time series extracted from the $X_t = 52\lambda_p$ converged wave series exhibits 3 events verifying $H_c/H_s > 1$ while for the other two series, no crest is higher than the significant wave height. Note that for this small time window (duration of $500s = 440T_p$), no rogue waves (defined as $H_c/H_s > 1.25$) are observed.

Lastly, Tab. 4 summarizes the main statistical parameters at the target location for each converged series. The presented values are averages of all the realizations. The kurtosis, the crest height at $POE = 10^{-3}$, the wave height at $POE = 10^{-3}$ and the two groupiness factors significantly increase with $X_t$. Therefore, the target location directly influences the severity of the wave fields. This has major consequences for the design tests of offshore structures. However, this phenomenon is only partially considered in usual industry practices (Det Norske Veritas, 2010; ITTC, 2011; Fouques et al., 2021).

## 6. Conclusion

The work presented in this paper deals with the generation of sea states at specified locations in experimental wave tanks, the main objective being to study the statistical properties of the waves depending on the target location.

First, a wave maker motion correction procedure was experimentally implemented to consecutively generate a typical not breaking sea state at three target locations of the ECN towing tank.

For the three experiments, high order non linear phenomena such as modulational instabilities and four-waves near-resonant interactions have been identified. The number of extreme events and the groupiness of the wave field significantly increase with the distance from the wave maker, resulting in i) a strong departure of crest and wave height distributions from reference benchmarks at the end of the tank and ii) a free surface elevation kurtosis increase along the domain. The latter can be partially modelled and predicted using a theoretical framework based on NLS equations for water waves (Janssen, 2003). Note that the distribution of wave periods is not influenced by the propagating distance. The periods of the extreme waves observed far from the wave maker are not extreme. They stand close to $T_1$, around to the most probable periods of the measured zero-crossing waves.

The variations of the input spectrum, resulting from the correction procedure, mainly correct the spectrum at the target location but do not significantly affect the wave statistics and the wave field groupiness. Thus, wave fields associated with the same qualified spectrum but different statistics and groupiness have been generated. Depending on the target location, even if the spectrum is qualified the severity of the wave field significantly differs.

The emergence of a larger number of extreme events for larger $X_t$ cannot be detected by focusing only on the quality of the wave spectrum. However, the consequences on offshore structure design tests are likely to be significant. Consequently, offshore engineering wave qualification procedures need to incorporate the influence of the target location and to adapt the criteria on wave height statistics, taking into account the existence of large departures from usual crest height reference distributions. In this perspective, groupiness factors appear as useful tools to qualify the severity of the wave field. Note that the influence of both breaking and directionality, not studied in the present paper, should also be explored.

The control of both spectral and statistical properties of the wave field in a wave tank environment is an intricate challenge, as the control of the spectrum at a target location is insufficient. Note that two approaches have been recently suggested to tackle this issue. First, some work has been recently carried out to add pre-designed extreme events in the wave field in order to artificially ensure the emergence of stronger crest distributions (Lu et al., 2019). Then, work in progress aims at controlling the shape of the crest height distribution for a given target location, through the use of adapted nonlinear wave maker motions.

## Acknowledgments

This study was carried out in the framework of the Chaire Hydrodynamique et Structure Marines CENTRALE NANTES - BUREAU VERITAS. We would like to thank the staff of the E.C.N wave tank facility Dr Félicien Bonnefoy, Anne Levesque, Jérémy Ohana, Laurent Davoust and Stéphane Lambert for their active and useful help.

## References

Annenkov, S.Y., Shrira, V., 2009. Evolution of kurtosis for wind waves. Geophysical Research Letters 36.

Benjamin, T.B., Feir, J.E., 1967. The disintegration of wave trains on deep water part 1. theory. Journal of Fluid Mechanics 27, 417–430.

Bitner-Gregersen, E.M., Gramstad, O., Magnusson, A.K., Malila, M., 2020. Challenges in description of nonlinear waves due to sampling variability. Journal of Marine Science and Engineering 8, 279.

Brown, L.D., Cai, T.T., DasGupta, A., 2001. Interval estimation for a binomial proportion. Statistical science , 101–117.

Buchner, B., Forristall, G., Ewans, K., Christou, M., Hennig, J., 2011. New insights in extreme crest height distributions: A summary of the 'crest'jip, in: International Conference on Offshore Mechanics and Arctic Engineering, pp. 589–604.

Canard, M., Ducrozet, G., Bouscasse, B., 2020. Generation of 3hr long-crested waves of extreme sea states with hos-nwt solver, in: ASME 2020 39th International Conference on Ocean, Offshore and Arctic Engineering, American Society of Mechanical Engineers Digital Collection.

Cherneva, Z., Tayfun, M., Guedes Soares, C., 2009. Statistics of nonlinear waves generated in an offshore wave basin. Journal of Geophysical Research: Oceans 114.

Christou, M., Ewans, K., 2014. Field measurements of rogue water waves. Journal of physical oceanography 44, 2317–2335.

Deike, L., Berhanu, M., Falcon, E., 2012. Decay of capillary wave turbulence. Physical Review E 85, 066311.

Det Norske Veritas, 2010. Environmental conditions and environmental loads, recommended practice dnv-rp-c205.

Dommermuth, D.G., 2021. Spilling breaking ocean waves and inverse energy cascades. ResearchGate preprint 1.

Ducrozet, G., Bonnefoy, F., Le Touzé, D., Ferrant, P., 2012. A modified high-order spectral method for wavemaker modeling in a numerical wave tank. European Journal of Mechanics-B/Fluids 34, 19–34.

van Essen, S., Lafeber, W., 2017. Wave-induced current in a seakeeping basin, in: International Conference on Offshore Mechanics and Arctic Engineering, American Society of Mechanical Engineers. p. V07BT06A021.

Fadaeiazar, E., Leontini, J., Onorato, M., Waseda, T., Alberello, A., Toffoli, A., 2020. Fourier amplitude distribution and intermittency in mechanically generated surface gravity waves. Physical Review E 102, 013106.

Fedele, F., 2015. On the kurtosis of deep-water gravity waves. Journal of Fluid Mechanics 782, 25–36.

Fedele, F., Brennan, J., De León, S.P., Dudley, J., Dias, F., 2016. Real world ocean rogue waves explained without the modulational instability. Scientific reports 6, 27715.

Forristall, G.Z., 2000. Wave crest distributions: Observations and second-order theory. Journal of physical oceanography 30, 1931–1943.

Forristall, G.Z., 2017. Joint wave height and period statistics from linear simulations. Journal of Ocean Engineering and Marine Energy 3, 221–231.

Fouques, S., Eloïse, C., Lim, H.J., Kim, J., Canard, M., Ducrozet, G., Bouscasse, B., Koop, A., Zhao, B., Wang, W., Bihs, H., 2021. Qualification criteria for the verification of numerical waves - part 1: Potential-based numerical wave tank (pnwt), in: ASME 2021 40th International Conference on Ocean, Offshore and Arctic Engineering, American Society of Mechanical Engineers Digital Collection.

Funke, E., Mansard, E., 1980. On the synthesis of realistic sea states, in: Coastal Engineering 1980, pp. 2974–2991.

Haller, M.C., Dalrymple, R.A., 1995. Looking for wave groups in the surf zone, in: Proc. Coastal Dynamics, pp. 81–92.

de Hauteclocque, G., Derbanne, Q., El-Gharbaoui, A., 2012. Comparison of different equivalent design waves with spectral analysis, in: International Conference on Offshore Mechanics and Arctic Engineering, American Society of Mechanical Engineers. pp. 353–361.

Haver, S., 2001. Evidences of the existence of freak waves, in: Rogue waves, pp. 129–140.

Huang, W., Dong, S., 2021. Statistical description of wave groups in three types of sea states. Ocean Engineering 225, 108745.

Huang, Z.J., Guo, Q., 2017. Semi-empirical crest distributions of long-crest nonlinear waves of three-hour duration, in: ASME 2017 36th International Conference on Ocean, Offshore and Arctic Engineering, American Society of Mechanical Engineers Digital Collection.

Huang, Z.J., Zhang, Y., 2018. Semi-empirical single realization and ensemble crest distributions of long-crest nonlinear waves, in: ASME 2018 37th International Conference on Ocean, Offshore and Arctic Engineering, American Society of Mechanical Engineers Digital Collection.

Hudspeth, R.T., Medina, J.R., 1989. Wave group analysis by the hilbert transform, in: Coastal Engineering 1988, pp. 884–898.

ITTC, 2011. Ittc's recommended procedures and guidelines:seakeeping experiments.

Janssen, P.A., 2003. Nonlinear four-wave interactions and freak waves. Journal of Physical Oceanography 33, 863–884.

Jensen, J.J., Capul, J., 2006. Extreme response predictions for jack-up units in second order stochastic waves by form. Probabilistic Engineering Mechanics 21, 330–337.

Kirezci, C., Babanin, A.V., Chalikov, D.V., 2021. Modelling rogue waves in 1d wave trains with the jonswap spectrum, by means of the high order spectral method and a fully nonlinear numerical model. Ocean Engineering 231, 108715.

Kit, E., Shemer, L., 1989. On dissipation coefficients in a rectangular wave tank. Acta Mechanica 77, 171–180.

Komen, G.J., Cavaleri, L., Donelan, M., Hasselmann, K., Hasselmann, S., Janssen, P., 1996. Dynamics and modelling of ocean waves. Dynamics and Modelling of Ocean Waves, by GJ Komen and L. Cavaleri and M. Donelan and K. Hasselmann and S. Hasselmann and PAEM Janssen, pp. 554. ISBN 0521577810. Cambridge, UK: Cambridge University Press, August 1996. , 554.

Latheef, M., Swan, C., 2013. A laboratory study of wave crest statistics and the role of directional spreading. Proceedings of the Royal Society A: Mathematical, Physical and Engineering Sciences 469, 20120696.

List, J.H., 1991. Wave groupiness variations in the nearshore. Coastal Engineering 15, 475–496.

Longuet-Higgins, M.S., 1952. On the statisticaldistribution of the height of sea waves. JMR 11, 245–266.

Lu, W., Li, J., Li, X., Tian, X., Wu, X., Zhang, X., 2019. Experimental investigation on the statistics of rogue waves under a random wave background. Ocean Engineering 186, 106075.

Mase, H., 1989. Groupiness factor and wave height distribution. Journal of waterway, port, coastal, and ocean engineering 115, 105–121.

Michel, G., Bonnefoy, F., Ducrozet, G., Prabhudesai, G., Cazaubiel, A., Copie, F., Tikan, A., Suret, P., Randoux, S., Falcon, E., 2020. Emergence of peregrine solitons in integrable turbulence of deep water gravity waves. Physical Review Fluids 5, 082801.

NWT Preparation Workgroup, 2019. Year 1 Report. Technical Report. JIP on Reproducible CFD Modeling Practice for Offshore Applications.

Onorato, M., Cavaleri, L., Fouques, S., Gramstad, O., Janssen, P.A., Monbaliu, J., Osborne, A.R., Pakozdi, C., Serio, M., Stansberg, C., et al., 2009. Statistical properties of mechanically generated surface gravity waves: a laboratory experiment in a three-dimensional wave basin. Journal of Fluid Mechanics 627, 235–257.

Onorato, M., Osborne, A.R., Serio, M., Cavaleri, L., Brandini, C., Stansberg, C., 2006. Extreme waves, modulational instability and second order theory: wave flume experiments on irregular waves. European Journal of Mechanics-B/Fluids 25, 586–601.

Onorato, M., Residori, S., Bortolozzo, U., Montina, A., Arecchi, F., 2013. Rogue waves and their generating mechanisms in different physical contexts. Physics Reports 528, 47–89.

Saulnier, J.B., Clément, A., António, F.d.O., Pontes, T., Prevosto, M., Ricci, P., 2011. Wave groupiness and spectral bandwidth as relevant parameters for the performance assessment of wave energy converters. Ocean Engineering 38, 130–147.

Serio, M., Onorato, M., Osborne, A.R., Janssen, P., et al., 2005. On the computation of the benjamin-feir index .

Shemer, L., Alperovich, L., 2013. Peregrine breather revisited. Physics of Fluids 25, 051701.

Shemer, L., Sergeeva, A., Liberzon, D., 2010. Effect of the initial spectrum on the spatial evolution of statistics of unidirectional nonlinear random waves. Journal of Geophysical Research: Oceans 115.

Tang, T., Adcock, T.A., 2021. The influence of finite depth on the evolution of extreme wave statistics in numerical wave tanks. Coastal Engineering 166, 103870.

Tayfun, M.A., 1990. Distribution of large wave heights. Journal of waterway, port, coastal, and ocean engineering 116, 686–707.

Welch, P., 1967. The use of fast fourier transform for the estimation of power spectra: a method based on time averaging over short, modified periodograms. IEEE Transactions on audio and electroacoustics 15, 70–73.

Zakharov, V.E., L'vov, V.S., Falkovich, G., 2012. Kolmogorov spectra of turbulence I: Wave turbulence. Springer Science & Business Media.

- Non breaking sea states can be generated at any specified location in a wave tank
- In wave tanks the wave height statistics depend on the distance from the wave maker
- A single wave energy spectrum can be associated with various wave height statistics

**M. Canard:** Conceptualization, Methodology, Validation, Formal analysis, Investigation, Data curation, Writing - original draft, Writing - review & editing, Visualization.

**G. Ducrozet:** Conceptualization, Methodology, Validation, Formal analysis, Investigation, Writing - original draft, Writing - review & editing , Supervision, Funding acquisition.

**B. Bouscasse:** Conceptualization, Methodology, Validation, Investigation, Data curation, Writing - review & editing, Supervision, Funding acquisition.

**Declaration of interests**

☒ The authors declare that they have no known competing financial interests or personal relationships that could have appeared to influence the work reported in this paper.

☐The authors declare the following financial interests/personal relationships which may be considered as potential competing interests:

G. Ducrozet

M. Canard